

An Iterative Scheme for the Solidification Benchmark Modeling

Xiaoyu Feng^{1,2}[0000–0002–0050–1919], Huangxin Chen³, Bo Yu⁴, and Shuyu Sun¹[0000–0002–3078–864X]

- ¹ Computational Mathematics, School of Mathematical Sciences, Tongi University, Shanghai 200092, China
- ² Computational Transport Phenomena Laboratory, Division of Physical Science and Engineering, King Abdullah University of Science and Technology, Thuwal 23955-6900, Saudi Arabia
xiaoyu.feng@kaust.edu.sa
- ³ School of Mathematical Sciences and Fujian Provincial Key Laboratory on Mathematical Modeling and High Performance Scientific Computing, Xiamen University, Fujian 361005, China
- ⁴ School of Petroleum Engineering, Yangtze University, Wuhan 430100, China
suns@tongji.edu.cn

Abstract. The processes of solidification and macro-segregation involve intricate interactions across multiple physical, phase, and compositional fields, including mass, momentum, energy, and material transfer. Accurate prediction of phase transitions, chemical heterogeneities, and compositional flows is crucial in fields such as materials science, energy science, and planetary science. Numerical benchmark studies provide an effective means to explore these phenomena. This paper presents an iterative scheme based on operator splitting and evaluates its accuracy, stability, and implementation through a relevant benchmark problem. The results demonstrate strong performance of the scheme, particularly in capturing key physical phenomena such as channel segregation, freckle formation, and edge effects.

Keywords: Solidification · Multi-phase · Operator-splitting · Iterative Scheme · Benchmark Modeling

1 Introduction

Solidification is a complex process involving the transfer of mass, momentum, energy, and species, with multi-phase and multi-component interactions. Key phenomena such as chemical heterogeneity, macro-segregation, and phase transitions between solid, mushy, and liquid regions are essential to understanding material behaviors in fields like material science [20], energy storage [11], magma ocean evolution [12], safe operation of pipelines [19] and the high-efficiency recovery of natural gas hydrate (NGH) from the subsurface [16].

Experimental studies using both opaque alloys (e.g., Al–Cu, Sn–Pb) and transparent analogs (e.g., NH_4Cl , Na_2CO_3) have provided valuable data and

made progress for deep understanding of this physical process [10,9]. Numerical simulation [15,22] is also a vital tool for understanding these complex processes, especially when time and space constraints limit experimental methods. These simulations are commonly based on mesh-free methods like SPH [8,7], moving-grid methods like ALE [2], and fixed-mesh methods such as VOF, level-set [17] and LBM [4]. Among these, the enthalpy-porosity methods [18,14] and the phase field methods [21] are widely used for solidification simulations due to their simplicity in dealing with phase transitions on a macroscale.

This paper introduces a novel iterative scheme based on operator-splitting and matrix-based methods, designed to improve convergence rates and computational efficiency. The scheme is validated through benchmark tests, demonstrating its capability to capture important physical phenomena such as macro-segregation and phase transitions [3,18]. Additionally, the integration of vectorization and forward matrix assembly techniques enhances the scalability and efficiency of the method, making it suitable for extending to 3D simulations.

The structure of the paper is as follows: Section 2 provides a concise summary of the classical models and their assumptions. Section 3 introduces and derives our proposed numerical scheme. Section 4 presents a classic benchmark example and discusses the validation results. Finally, Section 5 concludes the study with final remarks.

2 Mathematical model

The most fundamental and universal single-domain continuum mixture model is derived from mass averaging and classical mixture theory. This model suggests that the properties of the mixture are the result of the individual components, with its governing equations resembling those of the individual phases. It leverages the continuous phase transition of the mixture, represented by phase fractions, while ensuring the conservation of mass, momentum, energy, and components within the system. Since all governing equations follow a similar convection-diffusion form, by introducing a general scalar quantity ϕ_ω associated with phase ω in a multiphase system, the general physical relationship can be established. We define the partial volume density of phase for phase ω , namely $\bar{\rho}_\omega = \frac{V_\omega}{V} \frac{m_\omega}{V_\omega} = g_\omega \rho_\omega$ and $\bar{\rho}_\omega^\theta = \frac{V_\omega^\theta}{V_\omega} \frac{m_\omega^\theta}{V_\omega^\theta} = g_\omega^\theta \rho_\omega^\theta$ as the partial volume density of the component θ within phase ω .

Then we have the mass fraction of one phase $f_\omega = \frac{\bar{\rho}_\omega}{\sum_\omega \bar{\rho}_\omega}$. Then obviously the relations for the volume fraction and mass fraction as follows: $\sum_\omega f_\omega = 1$; $\sum_\omega g_\omega = 1$. Based on the mass-averaged velocities and general variables, the equations are as follows:

$$\mathbf{u} = \frac{1}{\rho} \sum_\omega \bar{\rho}_\omega \mathbf{u}_\omega = \sum_\omega f_\omega \mathbf{u}_\omega, \quad (1)$$

$$\phi = \frac{1}{\rho} \sum_\omega \bar{\rho}_\omega \phi_\omega = \sum_\omega f_\omega \phi_\omega, \quad (2)$$

where the density of one mixture is $\rho = \sum_{\omega} \bar{\rho}_{\omega}$. The conservation law for general scalar quantities can be written as:

$$\frac{\partial}{\partial t} \int_{\bar{V}} [\rho_{\omega} \phi_{\omega}] d\bar{V}_{\omega} + \int_S [\rho_{\omega} \mathbf{u}_{\omega} \phi_{\omega}] \cdot \mathbf{n} dS_{\omega} = \int_S \mathbf{J}_{\omega} \cdot \mathbf{n} dS_{\omega} + \int_{\bar{V}} S r_{\omega} d\bar{V}_{\omega}. \quad (3)$$

The terms correspond to the dynamic term, convection flux, diffusion flux, and the source term. Assuming smoothness and differentiability of the arguments under the surface integrals, the divergence theorem yields:

$$\frac{\partial}{\partial t} (\bar{\rho}_{\omega} \phi_{\omega}) + \nabla \cdot (\bar{\rho}_{\omega} \mathbf{u}_{\omega} \phi_{\omega}) = \nabla \cdot (g_{\omega} \mathbf{J}_{\omega}) + g_{\omega} S r_{\omega}. \quad (4)$$

The conservation of mass, momentum, energy and component relations can be referred by assigning the general quantities in the governing equation (4) with different variables and doing summation for all phases ω .

Generally, the above conservation relations are applicable for multiple phases and components. Here, we only consider the solid-liquid phase change ($\omega = l, s$) of the binary mixture ($\theta = A, B$). Based on the above identity, the model for solidification of this problem can be presented as:

Mass conservation:

$$\frac{\partial \rho}{\partial t} + \nabla \cdot (\rho \mathbf{u}) = 0, \quad (5)$$

where $\rho = g_s \rho_s + g_l \rho_l$, $\mathbf{u} = f_s \mathbf{u}_s + f_l \mathbf{u}_l$.

Momentum equation:

$$\frac{\partial(\rho \mathbf{u})}{\partial t} + \nabla \cdot (\rho \mathbf{u} \otimes \mathbf{u}) = -\nabla p + \nabla \cdot (\mu_l \frac{\rho}{\rho_l} \nabla \mathbf{u}) + \rho \mathbf{g} - \frac{\mu_l}{K} \frac{\rho}{\rho_l} (\mathbf{u} - \mathbf{u}_s), \quad (6)$$

where the body force is \mathbf{g} and the diffusion term can be derived with some trivial simplification, and the details can be referred to [3].

The flow in the mushy zone is considered laminar and Newtonian with constant viscosity, treated as an isotropic porous medium without direction coupling effects. Thus, the off-diagonal elements of the permeability tensor are zero. The phase interaction term, based on the Kozeny-Ångström-Carman formula with relative phase velocity, acts as a damping term in equation (6). The permeability for flow in the mushy region is given by:

$$K = \frac{\lambda_2^2 f_l^3}{180 (1 - f_l)^2}, \quad (7)$$

where λ_2 represents the secondary dendrite arm spacing, a key microstructural feature that influences inter-dendritic flow and is commonly used to determine permeability.

Energy equation:

$$\frac{\partial(\rho h)}{\partial t} + \nabla \cdot (\rho \mathbf{u} h) = \nabla \cdot (k \nabla T) - \nabla \cdot (\rho (h_l - h) (\mathbf{u} - \mathbf{u}_s)), \quad (8)$$

where enthalpy $h = f_s h_s + f_l h_l$ and the conductivity uses volume average instead of mass average, $k = g_s k_s + g_l k_l$, because it is related to the size of the material itself.

Defining average heat capacities $\bar{c}_{pl} = \frac{1}{T} \int_0^T c_{pl} dT$ and $\bar{c}_{ps} = \frac{1}{T} \int_0^T c_{ps} dT$, the solid and liquid phase enthalpies are

$$h_s = \int_0^T c_{ps} dT + h_s^0 = \bar{c}_{ps} T, \quad h_l = \int_0^T c_{pl} dT + h_l^0 = \bar{c}_{pl} T + L,$$

where we set $h_s^0 = 0$ and $h_l^0 = L$, L is the latent heat of phase change. Based on the mass average of heat capacity $\bar{c}_p = f_s \bar{c}_{ps} + f_l \bar{c}_{pl}$, then we can easily arrive at

$$h = \bar{c}_p T + f_l L, \quad (9)$$

Transport equation:

$$\frac{\partial(\rho C)}{\partial t} + \nabla \cdot (\rho \mathbf{u} C) = \nabla \cdot (\rho f_l D_l \nabla C) + \nabla \cdot (\rho f_l D_l \nabla (C_l - C)) - \nabla \cdot (\rho (C_l - C) (\mathbf{u} - \mathbf{u}_s)). \quad (10)$$

Considering the binary solid-liquid system, for the sake of conciseness of the notation, C represents the concentration (or mass fraction) of the primary solute of the binary mixture system. The diffusion in the solid phase can be ignored compared with the liquid phase ($D_l^A \gg D_s^A$). With this assumption and the identity $\nabla C_l = \nabla C + \nabla (C_l - C)$, (10) can be deduced.

Lever rule:

The component conservation and the constraint on mass fraction for the binary solid-liquid system indicate:

$$C = f_l C_l + f_s C_s. \quad (11)$$

$$f_l + f_s = 1. \quad (12)$$

Then, the "lever rule" can be deduced as:

$$\begin{cases} f_s = \frac{C_l - C}{C_l - C_s}, \\ f_l = \frac{C - C_s}{C_l - C_s}. \end{cases} \quad (13)$$

The implication of the "lever rule" can be easily appreciated from the above equations. They describe the relationship between the mass fraction of the component and the phase fraction in a binary system.

Phase equilibrium relation:

For this dynamic problem, even the local thermodynamic equilibrium has been assumed, but the phase equilibrium relations still need to be specified to ensure the closure of the PDE system. Usually, this relation is characterized by the equation of state (EoS). The van der Waals (VdW) EoS or Peng-Robinson (PR) EoS is widely recognized for gas-liquid problems [6]. Generally, the solute fraction and phase fraction can be determined based on the EoS and the constraints. While there is no widely accepted EoS model for the solid-liquid problem,

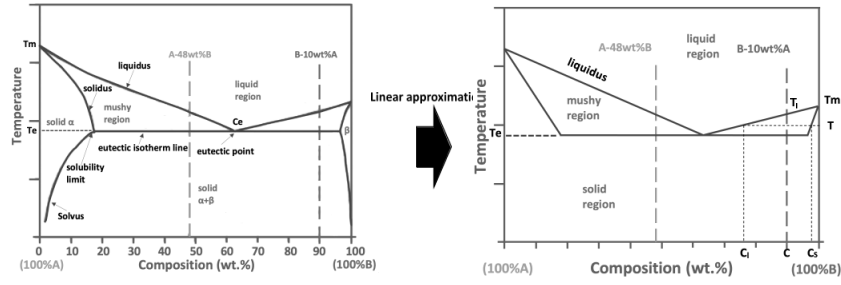


Fig. 1. Linear approximation of the phase diagram

the phase diagram from experiments with some approximations are still used as the basis for simulation. Combining the "lever rule" with the phase diagram, C_l , C_s and f_l , f_s can be determined with certain T and C .

Simplified model:

- The velocity of the solid phase is zero ($\mathbf{u}_s = \mathbf{0}$).
- Heat capacities of both phases are constant and equal ($c_{pl} = c_{ps} = c_p$).
- The densities of liquid and solid phases are equal and constant, thus $f_l = g_l$; $f_s = g_s$.
- The thermal and solutal driven buoyancy body forces are characterized by the Boussinesq approximation: $\Delta\rho = (-\beta_T (T - T_{ref}) - \beta_c (C_l - C_{ref})) \rho_0$.
- The linear approximation of the phase diagram is shown in Figure 1 (the slopes for the liquidus and solidus lines are fixed, and they correspond to k_p and \mathcal{L} being constants).

Then, the simplified and reduced model can be expressed as follows:

$$\nabla \cdot \mathbf{u} = 0, \quad (14a)$$

$$\frac{\partial \mathbf{u}}{\partial t} + (\mathbf{u} \cdot \nabla) \mathbf{u} = \nabla \cdot \left(\frac{\mu_l}{\rho_0} \nabla \mathbf{u} \right) - \frac{1}{\rho_0} \nabla p - \frac{\mu_l}{\rho_0} K^{-1} \mathbf{u} + \frac{(\rho_0 + \Delta\rho)}{\rho_0} \mathbf{g}, \quad (14b)$$

$$\frac{\partial T}{\partial t} + \nabla \cdot (\mathbf{u} T) = \nabla \cdot \left(\frac{k}{\rho_0 c_p} \nabla T \right) - \frac{L}{c_p} \frac{\partial g_l}{\partial t}, \quad (14c)$$

$$g_l = 1 - \frac{1}{1 - k_p} \frac{T - T_l}{T - T_m}, \quad (\text{where } T_l = \mathcal{L}C + T_m), \quad (14d)$$

$$\frac{\partial C}{\partial t} + \nabla \cdot (\mathbf{u} C_l) = \nabla \cdot (g_l D_l \nabla C_l), \quad (14e)$$

$$C_l = \frac{C}{1 - (1 - k_p)(1 - g_l)}. \quad (14f)$$

Then unknowns become $\mathbf{u}, p, T, C, C_l, g_l$ and they can be determined by the above system with 6 equations.

3 Numerical scheme

On the basis of the aforementioned mathematical model (14), an iterative numerical scheme are proposed and the classical fully decoupled scheme is also presented as comparison. In this section, operator-splitting and matrix-based techniques are employed for constructing the schemes. The sequence of numerical solutions follows the real physical process: the cooling is the fundamental startup source, then local phase equilibrium is assumed and T, g_l are strong couplings, the temperature is determined by the energy equation, then the thermal and solutal driven force induces the flow, and the flow will eventually cause the transport of the component. Thus, the temporal discretization is given in this order. The superscripts $n + 1$ and n represent implicit and explicit terms, respectively.

3.1 The operator-splitting method for energy equation:

In this part, schemes are designed to solve the energy equation and to handle the local phase equilibrium relation concurrently, namely the strong coupling effect between the temperature and phase fraction.

A fully decoupled scheme for the energy equation:

The solution procedure for the energy equation is split into two steps: first step takes into account heat convection and diffusion,

$$\frac{T^* - T^n}{\Delta t} + \mathbf{u}^n \cdot \nabla T^* = \nabla \cdot \left(\frac{k}{\rho_0 c_p} \nabla T^* \right). \quad (3.1)$$

The second step is responsible for the correction of latent heat when a phase transition occurs,

$$\frac{T^{n+1} - T^*}{\Delta t} = -\frac{L}{c_p} \frac{g_l^{n+1} - g_l^n}{\Delta t}. \quad (3.2)$$

The phase equilibrium relations yields:

$$g_l^{n+1} = 1 - \frac{1}{1 - k_p} \frac{T^{n+1} - T_l(C^n)}{T^{n+1} - T_m}, \quad (3.3)$$

and

$$T_l = T_m + \mathcal{L}C^n, \quad (3.4)$$

where T_l corresponds to the liquidus temperature at the current concentration C . Because of the segregation process, the deviation of concentration C^n from the uniform concentration C_0 will result in a range of $T_l(C^n)$ across the entire computational domain. Then, by substituting it in the second step of operator-splitting expressions, a quadratic equation of the liquid volume fraction g_l^{n+1} will be found:

$$a \cdot (g_l^{n+1})^2 + b \cdot g_l^{n+1} + c = 0, \quad (3.5)$$

where coefficients are

$$\begin{cases} a = 1 - k_p, \\ b = k_p - g_l^n (1 - k_p) + \frac{c_p}{L} (1 - k_p) (T_m - T^*), \\ c = - (g_l^n + \frac{c_p}{L} T^*) k_p + \frac{c_p}{L} (T_l - (1 - k_p) T_m). \end{cases} \quad (3.6)$$

By employing the bound $[0, 1]$ for the phase fraction and the truncation operation for the root, the unique solution for g_l will be obtained. It must be emphasized that the second step is crucial for accurately quantifying the change in temperature when it involves the phase change and the latent heat releases. The second step will also determine T^{n+1} . It is worth remarking that the cooling decreases temperature and cancels the latent heat at the initial stage, but when it comes to the eutectic temperature, phase change will occur isothermally; that is, the temperature at any point can only decrease once the material at that point has solidified completely.

An iterative scheme for the energy equation:

The fully decoupled scheme loses accuracy to some extent, while solving nonlinear systems directly is not expected. So, based on the operator-splitting idea, an iterative scheme is proposed here to enhance the accuracy at each time step. Given a tolerance ϵ and $T_0^{n+1} = T^n$. For $q \geq 0$, firstly we solve

$$\frac{\hat{T}_{q+1}^{n+1} - T^n}{\Delta t} + \nabla \cdot (\mathbf{u}^n T_q^{n+1}) = \nabla \cdot \left(\frac{k}{\rho_0 c_p} \nabla T_q^{n+1} \right) - \frac{L}{c_p} \frac{g_{l,q+1}^{n+1} - g_l^n}{\Delta t}, \quad (3.7)$$

where the subscript q represents the iteration number at the current time step. After we get the \hat{T}_{q+1} from the first step, Secondly, we solve

$$\frac{T_{q+1}^{n+1} - \hat{T}_{q+1}^{n+1}}{\Delta t} + \nabla \cdot (\mathbf{u}^n T_{q+1}^{n+1} - \mathbf{u}^n T_q^{n+1}) = \nabla \cdot \left(\frac{k}{\rho_0 c_p} \nabla T_{q+1}^{n+1} - \frac{k}{\rho_0 c_p} \nabla T_q^{n+1} \right). \quad (3.8)$$

As the iteration progresses, if the difference between T_{q+1}^{n+1} , T_q^{n+1} and \hat{T}_{q+1} becomes sufficiently small, then it is considered convergence. The convergence criteria is set: $\|T_{q+1}^{n+1} - T_q^{n+1}\|_{L^\infty} \leq \epsilon$ and $\|T_{q+1}^{n+1} - \hat{T}_{q+1}^{n+1}\|_{L^\infty} \leq \epsilon$ both hold. Otherwise, we continue the iteration by setting $q := q + 1$ and going back to compute a new T_{q+1}^{n+1} .

Remark 1. In the first step, solving the quadratic equation of the liquid fraction is still necessary. In contrast with a fully decoupled one, the coefficient b will be updated by $b := b - \frac{c_p}{L} (1 - k_p) \Delta t \gamma_q$ and c will be updated by $c := c - \frac{c_p}{L} k_p \Delta t \gamma_q$, where $\gamma_q = \nabla \cdot \left(\frac{k}{\rho c_p} \nabla T_q^{n+1} \right) - \nabla \cdot (\mathbf{u}^{n+1} T_q^{n+1})$.

3.2 The semi-implicit pressure correction method for momentum equation:

$$\frac{\mathbf{u}^{n+1} - \mathbf{u}^n}{\Delta t} + \mathbf{u}^n \cdot \nabla \mathbf{u}^{n+1} = \nabla \cdot \left(\frac{\mu_l}{\rho_0} \nabla \mathbf{u}^{n+1} \right) - \frac{1}{\rho_0} \nabla p^{n+1} - \frac{\mu_l}{\rho_0} K^{-1} \mathbf{u}^{n+1} + \frac{(\rho_0 + \Delta \rho)}{\rho_0} \mathbf{g}, \quad (3.9)$$

$$\nabla \cdot \mathbf{u}^{n+1} = 0. \quad (3.10)$$

The pressure correction scheme is used for solving velocity. Combining the divergence-free condition with the momentum equation gives

$$\frac{\mathbf{u}^* - \mathbf{u}^n}{\Delta t} + \mathbf{u}^n \cdot \nabla \mathbf{u}^* = \nabla \cdot \left(\frac{\mu_l}{\rho_0} \nabla \mathbf{u}^* \right) - \frac{1}{\rho_0} \nabla p^n - \frac{\mu_l}{\rho_0} K^{-1} \mathbf{u}^* + \frac{(\rho_0 + \Delta \rho)}{\rho_0} \mathbf{g}, \quad (3.11)$$

and the pressure correction Poisson equation

$$\nabla^2 (p^{n+1} - p^n) = \frac{\rho_0}{\Delta t} \nabla \cdot \mathbf{u}^*. \quad (3.12)$$

Then the velocity can be updated through pressure correction:

$$\frac{\mathbf{u}^{n+1} - \mathbf{u}^*}{\Delta t} = -\frac{1}{\rho_0} \nabla (p^{n+1} - p^n) \quad (3.13)$$

3.3 The matrix-based technique for the species transport equation:

$$\frac{C^{n+1} - C^n}{\Delta t} + \nabla \cdot (\mathbf{u}^{n+1} C_l^{n+1}) = 0, \quad (3.14)$$

If we consider the diffusion effect in the liquid phase as well, we have

$$\frac{C^{n+1} - C^n}{\Delta t} + \nabla \cdot (\mathbf{u}^{n+1} C_l^{n+1}) = \nabla \cdot (g_l D_l \nabla C_l^{n+1}). \quad (3.15)$$

It must be noted that convection terms in the momentum equation, transport equation, and energy equation are all treated with an upwind implicit scheme. However, the main difficulty caused by the transport equation comes from C_l^{n+1} in the convection and diffusion terms, which differ from C^{n+1} in the temporal term. According to the explicit relationship between C_l and C :

$$C_l^{n+1} = \frac{C^{n+1}}{1 - (1 - k_p)(1 - g_l^{n+1})}, \quad (3.16)$$

in matrix form like:

$$C_l^{n+1} = \mathbf{A}_g C^{n+1}, \quad (3.17)$$

where \mathbf{A}_g is a diagonal matrix. Given the upwind coefficient matrix \mathbf{A}_{con} and the Laplacian coefficient matrix \mathbf{A}_{lap} , the temporal discrete transport equation in matrix and vector form can be expressed as:

$$\left(\frac{1}{\Delta t} \mathbf{I} + \mathbf{A}_{con} * \mathbf{A}_g - \mathbf{A}_{lap} * \mathbf{A}_g \right) C^{n+1} = \mathbf{rhs}, \quad (3.18)$$

where \mathbf{I} is the identity matrix. The notation \mathbf{rhs} denotes the right-hand side vector of the linear system.

This method with fully implicit scheme for C will enhance numerical stability and accuracy without introducing more explicit information of C^n in the discretization of the last two terms in the original expression used in traditional methods:

$$\frac{\partial C}{\partial t} + \nabla \cdot (\mathbf{u}C) = \nabla \cdot (g_l D_l \nabla C) + \nabla \cdot [g_l D_l \nabla (C_l - C)] - \nabla \cdot [(C_l - C) \mathbf{u}].$$

3.4 Updating the concentration:

With the determined g_l^{n+1} and C^{n+1} , the C_l^{n+1} and C_s^{n+1} can be updated by

$$C_l^{n+1} = \frac{C^{n+1}}{1 + (1 - g_l^{n+1})(k_p - 1)}, \quad (3.19)$$

and

$$C_s^{n+1} = k_p C_l^{n+1}. \quad (3.20)$$

Now, the progress of single time step has been completed. The iterative scheme based on operator splitting and matrix-based techniques, enhances accuracy and numerical stability.

3.5 Spatial discretization:

The finite volume method based on staggered grids, as shown in Figure 2 is applied. The computational domain $\Omega = [0, l_x] \times [0, l_y]$ includes a finite number of rectangular subdivisions. The mesh vertex points are located at:

$$x_i = i * h_x, \quad i = 0, 1, \dots, n_x,$$

$$y_j = j * h_y, \quad j = 0, 1, \dots, n_y,$$

where n_x and n_y are the number of meshes in each direction and $h_x = l_x/n_x$ and $h_y = l_y/n_y$ are mesh sizes. Four sets of mesh points (west-east edge points, south-north edge, cell-centered, vertex) are defined:

$$E_{we} = \left\{ \left(x_i, \frac{y_{j-1} + y_j}{2} \right) \mid i = 0, 1, \dots, n_x; j = 1, 2, \dots, n_y \right\},$$

$$E_{sn} = \left\{ \left(\frac{x_{i-1} + x_i}{2}, y_j \right) \mid i = 1, 2, \dots, n_x; j = 0, 1, \dots, n_y \right\},$$

$$E_c = \left\{ \left(\frac{x_{i-1} + x_i}{2}, \frac{y_{j-1} + y_j}{2} \right) \mid i = 1, 2, \dots, n_x; j = 1, 2, \dots, n_y \right\},$$

$$E_v = \{(x_i, y_j) \mid i = 0, 1, \dots, n_x; j = 0, 1, \dots, n_y\}.$$

The east and north interfaces of one cell are considered the front interfaces. On the contrary, the west and south interfaces are the back interfaces. Next, we have the discretized spaces:

$$U_h = \{u : E_{we} \rightarrow \mathbb{R}\}, \quad V_h = \{v : E_{sn} \rightarrow \mathbb{R}\},$$

$$P_h = \{P : E_c \rightarrow \mathbb{R}\}, \quad N_h = \{interpolation : E_v \rightarrow \mathbb{R}\}.$$

U_h, V_h are for physical variables u, v and all other physical scalar quantities (pressure P , temperature T , concentration C , phase fraction g_l and g_s , etc.) correspond to P_h . The space N_h is for the interpolation of coefficients such as

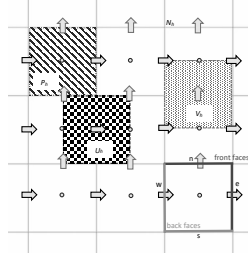


Fig. 2. Spatial discretization based on the staggered grid

μ . Multi-physical governing equations all obey the general convection-diffusion form:

$$\frac{\partial \phi}{\partial t} + \nabla \cdot (\mathbf{u}\phi) = \nabla \cdot (D\nabla\phi) + Sr(\phi), \quad (3.21)$$

where ϕ denotes a general physical variable and D is the general diffusion coefficient; the convection velocity is denoted by \mathbf{u} and $S_r(\phi)$ represents the source term. It is worth mentioning that, for the Darcy-like damping source term in the momentum equation, the fully implicit scheme for \mathbf{u}^{n+1} is vital as well, which corresponds to $S_r(\phi_{i,j}^{n+1})$ in (3.21).

4 Numerical Simulation

This section presents simulations and analyses of a numerical benchmark case using the proposed methods. The solidification and macro-segregation processes of two common binary alloy systems, Sn-10%Pb and Pb-48%Sn, are examined. Data on the physical properties of these two kinds of alloys can be referred to [1,18]. The findings on physical phenomena, as well as the evolution of velocity, temperature, phase fraction, and chemical component distributions, are presented. All numerical simulations were conducted on a MacOS Mojave system equipped with a 2.5GHz quad-core Intel Core i7 processor. The codes were developed from scratch using Matlab.

Example: solidification of Sn-10%Pb alloy in a 2D domain This benchmark case examines the solidification of a Sn-10%Pb binary alloy within a rectangular cavity [1]. The computational domain, initial conditions, and boundary conditions are illustrated in Figure 3. Initially, the cavity is filled with a still liquid alloy at a uniform temperature $T_0 = T_l$ and a consistent chemical concentration C_0 . At $t = 0$, the solidification process is triggered by cooling the left and right walls of the cavity via natural convection, described by the heat transfer coefficient h_T :

$$q_T = h_T(T - T_{\text{ext}}).$$

The top and bottom walls of the cavity are thermally insulated, and it is assumed that the cavity walls are rigid and nonslip. Phase transition occurs

within the cavity, with inner flow driven by thermal and solutal buoyancy forces. A central observation point E is established to track the evolution of the flow and concentration, allowing us to validate the accuracy of the proposed scheme.

Numerical results were obtained using a 150×180 mesh with a time step of $\Delta t = 5 \times 10^{-3}s$. Figures show the solidification process at $t = 5s, 38s, 168s, 350s$, depicting temperature, concentration, liquid fraction, velocity, streamlines, and phase interfaces. The $g_l = 0.99$ and $g_l = 0.01$ contours represent the liquid/mush and mush/solid interfaces.

At the initial stage of solidification ($t = 5s$ and $t = 38s$), thermal buoyancy dominates, causing intense downward flow near the liquid/mush interface, with a clockwise circulation inside the liquid (see Figures 4(a) and 5(a)). The Pb-enriched melt increases density, intensifying downward flow. At $t = 5s$, the liquid/mush interface follows the temperature contour, but by $t = 38s$, the interface deviates due to higher Pb concentration (see Figure 4(a), 6(b)).

From $t = 38s$ to $168s$, the high Pb concentration lowers the liquidus temperature, causing the bottom section to reach mush last. Severe flow transports Pb, forming a platform-shaped Pb-enriched region and raising it along the cavity’s centerline. The temperature gradient and component transport cause bending of liquid fraction contours, resulting in channel segregation (see Figure 5(c)).

At $t = 168s$, the channels develop, and most of the domain is mush, except for the left-bottom corner (see Figure 5(c)). A thin isothermal phase transition layer appears at the right-bottom corner signaling the approach of full solidification.

By $t = 350s$, the mush/solid interface reaches the center, and solidification completes by $t = 450s$, with the channel segregation pattern matching previous results [5,13] (see Figure 5(d), 7(b)). Figure 7(a) shows the velocity magnitude change at point E , which aligns well with our predictions, exhibiting two peaks and one valley. The first peak corresponds to the most intense upward flow, and the second peak, higher than the first, corresponds to the severe downward flow near the liquid/mush interface. The minimum velocity occurs when point E is at the center of the vortex.

Figure 7(b) shows the liquid fraction profile at point E . The final segregation results are consistent with those of Combeau et al. [5] and Shen et al. [13]. At

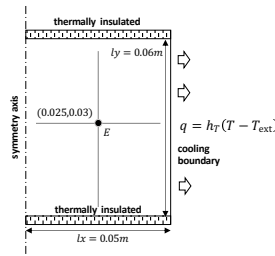


Fig. 3. Schematic of physical settings in Example 1

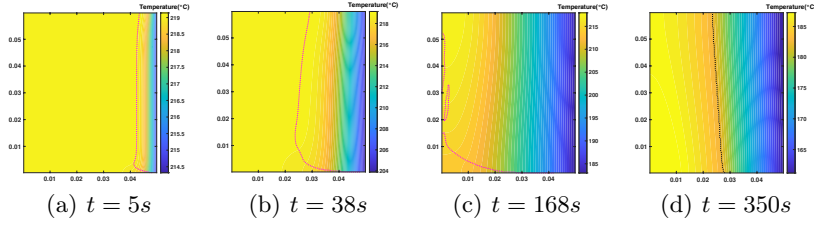


Fig. 4. Evolution of the temperature field with time; the liquid/mush interface (magenta dotted line); the mush/solid interface (black dotted line).

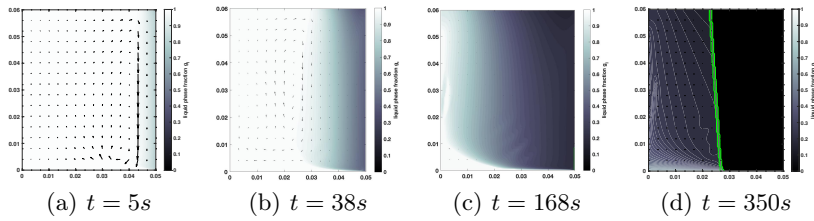


Fig. 5. Evolution of liquid fraction with time in Example 1; the iso-thermal phase transition layer (enclosed by green solid line); liquid fraction (colorbar).

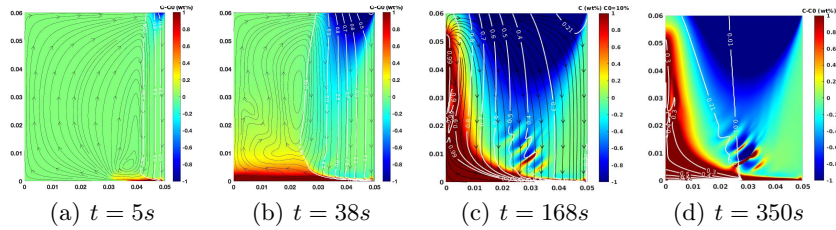


Fig. 6. Evolution of concentration variation $C - C_0$ with time; the liquid phase fraction contour line (white solid line); the streamline (black solid line with arrow); $C - C_0$ (colorbar)

around $t = 350s$, the liquid fraction drops sharply, indicating the transition from a non-isothermal to an isothermal process, with latent heat being released during phase change while the temperature remains constant until complete solidification. This confirms that our scheme effectively captures these critical properties and agrees with other benchmark results.

In Figure 4, the L_∞ norms of the differences among intermediate temperatures and temperatures of neighboring iterations decrease continuously. The convergence criteria are set to be $\epsilon = 10^{-6}$ and these two kinds of norms will be less than the criteria within 38 iterations. The iterative method can obtain more accurate results for each time step and less numerical error accumulated

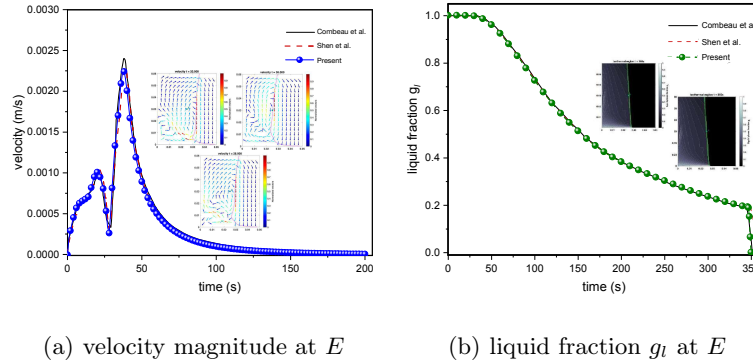


Fig. 7. (a) Time-dependent profile of velocity magnitude at central sample point E ; (b) time-dependent profile of liquid fraction g_l at central sample point E .

through the entire dynamic physical process. To assess the accuracy, we can examine the final segregation maps depicted in Figure 8. The patterns obtained from our fully decoupled code are like the results of Shen’s decoupled method [13]. The iterative scheme we employ yields a greater concentration of enrichment in the segregated channel layers, and the channel pattern is more agreeable to the results reported by Combeau et al. [5], which were simulated by high-order algorithms developed by the Institute Jean Lamour and the Fluent software.

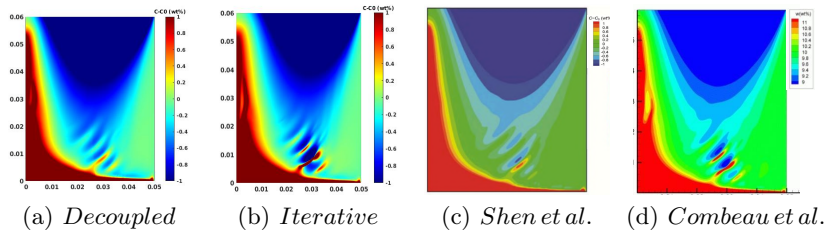


Fig. 8. The final segregation maps computed via (a) fully decoupled scheme; (b) iterative scheme; (c) and (d) are reference results from literature

5 Conclusions

This work presents a complete mathematical model for solidification and macro-segregation, emphasizing their broad applicability. We propose an iterative scheme and matrix-based methods to address these problems. A classic 2D benchmark case is presented to validate the accuracy and computational efficiency of the

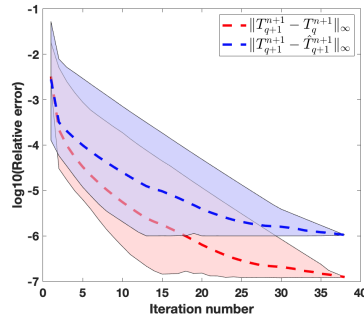


Fig. 9. Profile of the L_∞ norms with the number of iterations and their deviation (averaged by multiple time steps).

approach. The results computed by this iterative method demonstrate better convergence and accuracy compared to traditional fully decoupled methods, with contours showing good agreement with numerical results from high-order algorithms and commercial software. Future work can enhance this framework by incorporating real-phase equilibrium relations like equations of state.

Acknowledgments. This work is partially supported by King Abdullah University of Science and Technology (KAUST) through the grants BAS/1/1351-01, URF/1/5028-01. The work is also supported by National Key Research and Development Project of China (Grant Number: 2023YFA1011702), National Natural Science Foundation of China (Grant Numbers: 12122115, 51936001).

Disclosure of Interests. The authors declare that they have no known competing financial interests to influence the work reported in this paper.

References

1. Bellet, M., Combeau, H., Fautrelle, Y., Gobin, D., Rady, M., Arquis, E., Budenkova, O., Dussoubs, B., Duterrail, Y., Kumar, A., et al.: Call for contributions to a numerical benchmark problem for 2d columnar solidification of binary alloys. *International Journal of Thermal Sciences* **48**(11), 2013–2016 (2009)
2. Bellet, M., Fachinotti, V.D.: ALE method for solidification modelling. *Computer Methods in Applied Mechanics and Engineering* **193**(39-41), 4355–4381 (2004)
3. Bennon, W., Incropera, F.: A continuum model for momentum, heat and species transport in binary solid-liquid phase change systems—A model formulation. *International Journal of Heat and Mass Transfer* **30**(10), 2161–2170 (1987)
4. Chakraborty, S., Chatterjee, D.: An enthalpy-based hybrid lattice-boltzmann method for modelling solid-liquid phase transition in the presence of convective transport. *Journal of Fluid Mechanics* **592**, 155–175 (2007)
5. Combeau, H., Bellet, M., Fautrelle, Y., Gobin, D., Arquis, E., Budenkova, O., Dussoubs, B., Duterrail, Y., Kumar, A., Mosbah, S., et al.: A numerical benchmark on the prediction of macrosegregation in binary alloys. *Proceedings of frontiers in solidification science*. Warrendale, USA: TMS2011 (2011)

6. Feng, X., Chen, M.H., Wu, Y., Sun, S.: A fully explicit and unconditionally energy-stable scheme for Peng-Robinson VT flash calculation based on dynamic modeling. *Journal of Computational Physics* p. 111275 (2022)
7. Feng, X., Qiao, Z., Sun, S., Wang, X.: An energy-stable smoothed particle hydrodynamics discretization of the Navier-Stokes-Cahn-Hilliard model for incompressible two-phase flows. *Journal of Computational Physics* p. 111997 (2023)
8. Ghoneim, A.Y.: A smoothed particle hydrodynamics-phase field method with radial basis functions and moving least squares for meshfree simulation of dendritic solidification. *Applied Mathematical Modelling* **77**, 1704–1741 (2020)
9. Hachani, L., Zaidat, K., Fautrelle, Y.: Experimental study of the solidification of sn-10 wt.% pb alloy under different forced convection in benchmark experiment. *International Journal of Heat and Mass Transfer* **85**, 438–454 (2015)
10. Hebditch, D., Hunt, J.: Observations of ingot macrosegregation on model systems. *Metallurgical and Materials Transactions B* **5**(7), 1557–1564 (1974)
11. Hong, Y., Ye, W.B., Du, J., Huang, S.M.: Solid-liquid phase-change thermal storage and release behaviors in a rectangular cavity under the impacts of mushy region and low gravity. *International Journal of Heat and Mass Transfer* **130**, 1120–1132 (2019)
12. Kuritani, T.: Magmatic differentiation examined with a numerical model considering multicomponent thermodynamics and momentum, energy and species transport. *Lithos* **74**(3-4), 117–130 (2004)
13. Li, W., Shen, H., Liu, B.: A response to numerical benchmark for solidification of binary alloys: macro-segregation with thermo-solutal convection. *China Foundry* **9**(2) (2012)
14. Pardeshi, R., Voller, V., Singh, A., Dutta, P.: An explicit-implicit time stepping scheme for solidification models. *International Journal of Heat and Mass Transfer* **51**(13-14), 3399–3409 (2008)
15. Prakash, C., Voller, V.: On the numerical solution of continuum mixture model equations describing binary solid-liquid phase change. *Numerical Heat Transfer, Part B Fundamentals* **15**(2), 171–189 (1989)
16. Song, R., Feng, X., Wang, Y., Sun, S., Liu, J.: Dissociation and transport modeling of methane hydrate in core-scale sandy sediments: A comparative study. *Energy* **221**, 119890 (2021)
17. Sun, D., Tao, W.: A coupled volume-of-fluid and level set (VOSET) method for computing incompressible two-phase flows. *International Journal of Heat and Mass Transfer* **53**(4), 645–655 (2010)
18. Voller, V.R., Cross, M., Markatos, N.: An enthalpy method for convection/diffusion phase change. *International Journal for Numerical Methods in Engineering* **24**(1), 271–284 (1987)
19. Wang, M., Yu, G., Zhang, X., Zhang, T., Yu, B., Sun, D.: Numerical investigation of melting of waxy crude oil in an oil tank. *Applied Thermal Engineering* **115**, 81–90 (2017)
20. Wang, Z., Li, J., Liu, S., Zhao, J., Wang, X., Yang, W.: Investigation on freckle formation of nickel-based single crystal superalloy specimens with suddenly reduced cross section. *Journal of Alloys and Compounds* **918**, 165631 (2022)
21. Yang, X.: Efficient linear, stabilized, second-order time marching schemes for an anisotropic phase field dendritic crystal growth model. *Computer Methods in Applied Mechanics and Engineering* **347**, 316–339 (2019)
22. Zaeem, M.A., Yin, H., Felicelli, S.D.: Modeling dendritic solidification of al-3% cu using cellular automaton and phase-field methods. *Applied Mathematical Modelling* **37**(5), 3495–3503 (2013)